

Temperature influence on the production of nanodot patterns by ion beam sputtering of Si(001)

R. Gago,^{1,*} L. Vázquez,² O. Plantevin,^{3,4} J. A. Sánchez-García,² M. Varela,^{5,†} M. C. Ballesteros,⁵
J. M. Albella,² and T. H. Metzger⁴

¹*Centro de Micro-Análisis de Materiales and Departamento de Física Aplicada, Universidad Autónoma de Madrid, E-28049 Madrid, Spain*

²*Instituto de Ciencia de Materiales de Madrid, Consejo Superior de Investigaciones Científicas, E-28049 Madrid, Spain*

³*CSNSM CNRS/IN2P3, Université Paris-Sud, UMR8609, ORSAY-Campus, F-91405 Orsay Cedex, France*

⁴*Anomalous Scattering Beamline (ID-01), European Synchrotron Radiation Facility, F-38043 Grenoble Cedex, France*

⁵*Departamento de Física, Universidad Carlos III de Madrid, E-28911 Leganés, Spain*

(Received 26 October 2005; revised manuscript received 2 February 2006; published 11 April 2006)

The temperature influence ($T=300\text{--}625\text{ K}$) on the production of nanodot patterns by 1 keV Ar^+ ion beam sputtering (IBS) of Si(001) is addressed. The surface morphology was studied by atomic force microscopy, transmission electron microscopy, and grazing x-ray scattering techniques. Three different T regimes are observed: (i) First, the pattern does not change significantly up to 425 K, with the nanodot volume being mostly crystalline. (ii) Second, in the 425–525 K range, the pattern is still present but the nanodot height decreases with T and the crystalline core contribution to the dot morphology progressively diminishes. This trend is accompanied by a continuous decrease of the average interdot distance and an emerging strain in the crystalline lattice of the nanostructures. Above 500 K, the pattern is mainly dominated by the amorphous surface layer. (iii) Finally, the pattern formation is precluded above 550 K, yielding a flat and featureless surface. These results not only have technological implications regarding the control over the pattern characteristics, but also provide relevant information to contrast the existing theories of pattern formation by IBS.

DOI: [10.1103/PhysRevB.73.155414](https://doi.org/10.1103/PhysRevB.73.155414)

PACS number(s): 81.65.Cf, 81.16.Rf, 68.37.Ps, 61.10.Nz

I. INTRODUCTION

The production of nanocrystalline semiconductor structures has awakened great interest due to their application on optoelectronic and electronic devices. In particular, silicon nanostructures become very attractive because of their light-emitting properties¹ and their possible integration to current technological processes. In order to fabricate future devices the development of easy and industrially affordable preparation methods is mandatory. These methods should be compatible with large-scale production, allowing simultaneous control of purity, uniformity, and crystallinity of the nanostructures. Most employed nanostructuring methods consider top-down approaches such as chemical etching, x-ray lithography or electron beam techniques.² However, these techniques present some problems, such as lack of resolution and proximity effects. An alternative route consists in the use of self-organized methods allowing parallel processing and ordering of multiple nanostructures giving rise to a regular pattern. One of the most relevant examples of this type of processes is the Stranski-Krastanov growth of quantum dots.³

Recently, ion beam sputtering (IBS) has proved to be a competitive method for surface nanostructuring.⁴ This method allows to pattern large surface areas (several cm^2) after just a few minutes of ion irradiation. The potential of nanostructuring by IBS relies in its applicability to metals, semiconductors or insulators, and the additional control over the nanopattern features by changing the process parameters.⁴ The typical nanoscale topographies induced by IBS correspond to ripple⁵ or dot⁶ morphologies. In the case of amorphous materials or crystalline surfaces that become amorphous upon ion bombardment, ripples and dots are ob-

tained under off-normal or normal ion incidence, respectively. Nanodot patterns have also been achieved under off-normal ion incidence and simultaneous sample rotation.⁷ The characteristic wavelength of the patterns scales with the ion energy for both nanoripples⁸ and nanodots.⁹

Theoretically, the formation and evolution of surface nanostructures by IBS is described from the balance between smoothing processes and an instability induced by the dependence of the sputtering yield on the surface curvature.^{10–12} While the formation of ripple patterns has been known and studied experimentally⁵ and theoretically¹⁰ for some decades, the formation⁶ and description¹³ of regular dot arrays have gained attention only recently. In particular, the development of a theoretical framework, which can explain the experimental observations of nanodot pattern formation, is currently the subject of very active research.^{14–16} This effort needs to be complemented with experimental evidences in order to provide new and/or reliable data that can be contrasted with predictions from the theoretical models.

Among the relevant process parameters, temperature (T) can play a significant role in the nanostructuring process during IBS by governing surface diffusion processes. However, in contrast with other variables, the effect of T on the formation of nanodots by IBS has not been extensively studied. The lack of such studies responds mainly to experimental constraints to cover a wide temperature range. In the case of GaSb surfaces,⁹ no appreciable effects in the pattern formation were observed in the 213–333 K range, suggesting the dominance of ion induced diffusion processes.¹⁷ On the contrary, the production of InP nanodots within the 268–335 K range showed an increase of both interdot distance and dot height with T , and an interesting change in the pattern order-

ing from hexagonal-like to squarelike at 335 K.¹⁸ However, to date, no theoretical explanation has been given for the former observations.

Due to the technological relevance of silicon, we have focused our interest on the production of nanodot patterns on Si(001) surfaces by IBS.^{19,20} In particular, we address the influence of T on the surface topography within the relatively wide range of 300–625 K. The aim of this work is twofold. First, from a technological point of view, we address the eventual control of the pattern features by tuning the sample temperature. We draw special attention to the relative contribution of the crystalline and amorphous parts to the dot morphology by using advanced synchrotron radiation based methods. Second, this work provides experimental findings that can be contrasted with the existing theoretical models dealing with the IBS process.

II. CONTINUUM MODELS OF PATTERN FORMATION BY ION SPUTTERING

The most extended and successful theoretical approach for pattern formation on surfaces under ion beam erosion is based on the use of continuum equations to describe the evolution of interface roughening. In these models, the surface evolution is defined by a height function, $h(x, y, t)$, at any point (x, y) of the surface. In this way, the formation of ripples under ion beam erosion was first studied by Bradley and Harper¹⁰ (BH) using a certain partial differential equation. In the case of dot formation, the equation should be considered in its isotropic case,

$$\frac{\partial h(x, y, t)}{\partial t} = -v_0 - |\nu| \nabla^2 h(x, y, t) - D \nabla^4 h(x, y, t) \quad (1)$$

v_0 being the constant erosion velocity of the surface plane, ν the “effective surface tension” caused by the sputtering yield dependence on the surface curvature, and D the surface diffusion coefficient. The diffusion term accounts for thermal (K) and ion-induced (S) surface diffusion processes, resulting in an effective diffusion coefficient $D=S+K$.¹⁷ The thermal self-diffusion coefficient is given by $K=D_s C \gamma \Omega^2 / k_B T$, where D_s is the surface diffusivity, C is the surface concentration of mobile species, γ is the surface free energy per area, Ω is the atomic volume, k_B is the Boltzmann constant, and T is the temperature. The $D_s C$ factor can be expressed as $D_s C = A \exp(-\Delta E / k_B T)$, where A is a constant and the activation energy, $\Delta E = E_M + E_F$, is the sum of the migration (E_M) and formation (E_F) energies of mobile species. The contribution to A from the surface diffusivity is $d^2 f / 4$,²¹ where d is the lattice spacing of mobile species and f is the hopping frequency. The ion-induced diffusion mechanism does not imply mass transport along the surface and, thus, the magnitude of S is independent of T (i.e., it is not thermally activated).

Equation (1) predicts that a spatial frequency k_c grows exponentially faster than the other wavelengths from a random initial condition with a rate $R_k = -|\nu| k^2 - D k^4$. The maximum growth rate, $R_{k, \max} = \nu^2 / 4D$, occurs at the characteristic wave vector k_c , maximizing R_k and leading to the production

of a pattern with a characteristic wavelength $l_c = 2\pi \sqrt{2D / |\nu|}$. The values of ν and S can be related with physical parameters of the ion sputtering process through the Sigmund²² theory of sputtering, resulting in^{10,17}

$$\nu = -\frac{v_0 a \mu^2}{2\sigma^2} \text{ and } S = \frac{v_0 a \mu^4}{8\sigma^2}, \quad (2)$$

a being the average ion penetration range and σ and μ the lateral and longitudinal straggling of the deposited energy distribution, respectively.

Equation (1) reproduces qualitatively some of the experimental observations but still cannot account for several issues such as the stabilization of the pattern formation, coarsening of the characteristic wavelength with time or the self-organized ordering of the patterns. In order to explain the stabilization of the pattern, the BH theory has been generalized to include nonlinear and noise terms as follows^{11–13}

$$\begin{aligned} \frac{\partial h(x, y, t)}{\partial t} = & -v_0 - |\nu| \nabla^2 h(x, y, t) - D \nabla^4 h(x, y, t) \\ & + \lambda_1 [\nabla h(x, y, t)]^2 + \eta(x, y, t). \end{aligned} \quad (3)$$

Equation (3) is a noisy generalization of the Kuramoto-Sivashinski (KS) equation, where λ_1 is the coefficient of the nonlinear term and η is a white noise that reflects the stochastic nature of the erosion process. The nonlinear contribution comes from the tilt dependence of the sputtering yield at increasing slopes and, therefore, becomes dominant at long time scales.¹¹ Recently, in order to describe the self-organized ordering in the pattern formation, two new equations have been put forward. First, the damped version of the KS (DKS) equation has been proposed by Facsko *et al.*,¹⁵ where a damping term, $\partial_t h = -\alpha h$, is added to Eq. (3). The authors justify phenomenologically the inclusion of the damping term by additional physical mechanisms such as redeposition of sputtered material on the surface. Second, a promising approach different from the KS and DKS equations has been proposed by Castro *et al.*,¹⁴ in which both redeposition *and* surface viscous flow effects are highlighted. This theory is able to overcome many of the shortcomings of the KS equation by exploiting an analogy suggested between the surface sputtering process and the formation of aeolian sand ripples.²³ This approach explains both self-ordering and coarsening and allows deriving the following expression:

$$\frac{\partial h}{\partial t} = -|\nu| \nabla^2 h - D \nabla^4 h + \lambda_1 (\nabla h)^2 - \lambda_2 \nabla^2 (\nabla h)^2. \quad (4)$$

Some of the coefficients of Eq. (4) resemble those derived from the BH and KS frameworks, although they also include contributions from additional physical mechanisms related to the ion sputtering process. A detailed description of these terms can be found in Ref. 14.

III. EXPERIMENTAL DETAILS

A. Nanopattern production

Si(001) substrates were sputtered with 1 keV Ar⁺ ions at normal incidence for a total time of 10 min such that the

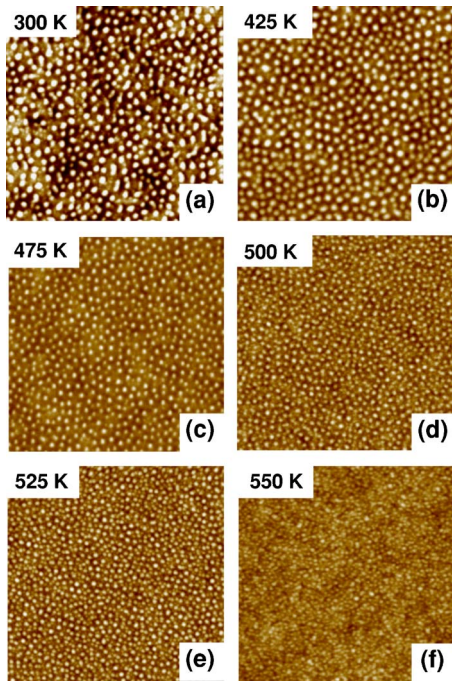


FIG. 1. (Color online) AFM $1 \times 1 \mu\text{m}^2$ images of Si(001) substrates sputtered with 1 keV Ar^+ ions during 10 min under normal incidence at (a) 300 K, (b) 425 K, (c) 475 K, (d) 500 K, (e) 525 K, and (f) 550 K.

surface morphology has reached a stationary state.¹⁹ The experiments were performed in a high vacuum chamber with a residual pressure of 10^{-7} mbar. The ion beam was extracted from a 3 cm commercial Kaufman ion source located 15 cm away from the substrate. In all the experiments, the working pressure was set to 2×10^{-4} mbar and the ion current density was fixed at $\sim 240 \mu\text{A}/\text{cm}^2$ (ion dose of $\sim 9 \times 10^{17}$ ions/ cm^2). The sputtering process was performed at T between 300 and 625 K by heating the samples with a resistive furnace in direct contact with their back side. The temperature was monitored *in situ* with a thermocouple attached to the sample holder. The sample produced at 300 K indicates that no intentional heating was applied, although the ion bombardment increases the sample T around 50–70 K. This additional heating was only observed for samples produced below ~ 400 K.

B. Pattern characterization

The surface morphology was imaged by atomic force microscopy (AFM) and transmission electron microscopy (TEM). AFM measurements were performed in air, operating in tapping mode with silicon cantilevers (nominal radius of 10 nm) with Nanoscope IIIa equipment (Veeco). Cross-sectional specimens suitable for high resolution TEM (HR-TEM) were prepared by a sequential procedure of mechanical grinding, dimpling, and argon ion milling at an acceleration voltage of 4 kV and an incidence angle of 12° . The TEM images were acquired using a Philips CM200 FEG analytical microscope operating at 200 kV.

Synchrotron experiments were carried out at the Anomalous Scattering Beamline (ID01) of the European Synchro-

tron Radiation Facility (ESRF) using a wavelength of 1.55 \AA ($E=8 \text{ keV}$). On the one hand, grazing incidence diffraction (GID) was performed at an incidence angle of $\alpha_i=0.2^\circ$, slightly below the critical angle for total external reflection $\alpha_c=0.22^\circ$, to enhance the scattered intensity. In this configuration, only the crystalline part of the dot is sampled. The momentum transfer (Q) dependent intensity around the in-plane Si(220) Bragg reflection was acquired with a linear position sensitive detector mounted perpendicular to the sample surface. In GID angular scans (Q perpendicular to the reciprocal lattice vector), the scattered intensity can be described as a product of a form factor and an interdot correlation function, allowing for simultaneous measurement of the dot size and ordering. In the strain sensitive radial direction (Q parallel to the reciprocal lattice vector), the GID intensity distribution is in addition affected by the strain modulation of the lattice parameter inside the dots or within the substrate near the surface.²⁴ On the other hand, grazing incidence small angle x-ray scattering (GISAXS) scans were recorded with a two-dimensional (2D) charged-coupled device (CCD) camera positioned in the forward direction to measure the scattered signal around the reflected beam. The angle α_i was set at 0.2° to enhance the signal, as in the case of GID, and the GISAXS spectra were extracted by horizontal cuts of the 2D image corresponding to $\alpha_f=0.3^\circ$. Complementary to GID, the Q dependence of the GISAXS signal is sensitive to the lateral correlation and the complete dot morphology, i.e., including crystalline and amorphous parts.

IV. EXPERIMENTAL RESULTS

A. Atomic force microscopy (AFM)

Figure 1 shows the AFM images of Si(001) surfaces bombarded with 1 keV Ar^+ under normal incidence for a total time of 10 min at different T . The formation of an induced surface pattern of nanodots can be clearly observed in the T range spanning from 300 K up to 525 K. At 300 K, the pattern consists of short-range hexagonal ordered arrays of nanodots with a lenticular shape (40–50 nm width and 5–6 nm height). Above 500 K, the pattern becomes less ordered and more packed.

Figure 2 shows the power spectral density (PSD) curves obtained from the AFM images of Fig. 1. The presence of a broad peak indicates a characteristic length in the pattern, which is related to the interdot distance. It is clear from both the AFM images and the PSD curves that the average interdot distance remains constant up to 425 K, but decreases (i.e., the PSD peak shifts to higher k values) continuously up to 525 K. The peak in the PSD curves disappears for $T \geq 550$ K, in agreement with the flat morphology observed in Fig. 1(f).

Figure 3 shows the evolution with substrate temperature of the average dot height, interdot distance, surface roughness, and surface dot density, as quantified from the analysis of the AFM images and PSD curves. From these data, we can distinguish three regions in the temperature series: (i) at low temperatures (<400 K), the pattern characteristics are not significantly affected; (ii) at intermediate temperatures (400–550 K), the dot morphology is still present but the dot

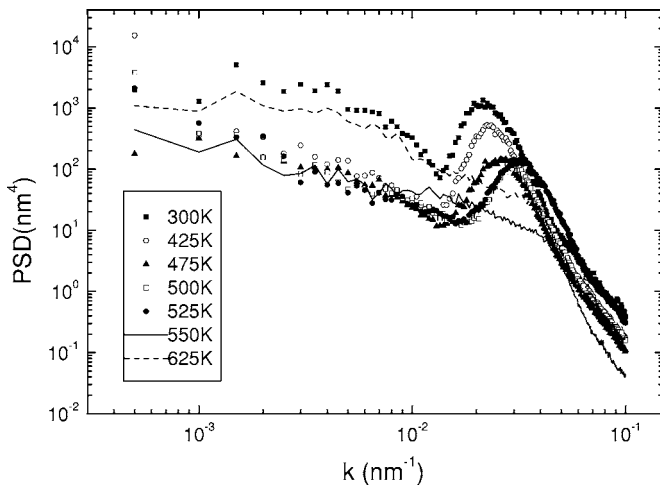


FIG. 2. PSD versus k plots obtained from the AFM images of Fig. 1. The corresponding substrate temperatures are: 300 K (■), 425 K (○), 475 K (▲), 500 K (□), 525 K (●), 550 K (solid line), and 625 K (dashed line).

height and, accordingly, the surface roughness decrease; and (iii) at high temperatures (550–650 K), the nanodot production is inhibited and the surface becomes flat. The decrease in the interdot distance previously indicated in Fig. 2 takes place in the intermediate temperature region, which gives rise to a higher dot density, as evidenced by the more packed pattern directly observed from the AFM images.

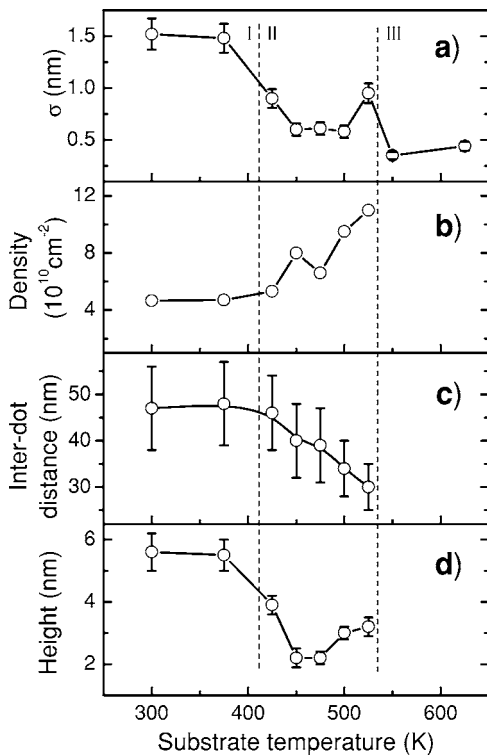


FIG. 3. Dependence of surface roughness (a), dot density (b), average interdot distance (c), and average dot height (d), as obtained from the AFM data, on the substrate temperature for Si(001) substrates bombarded by 1 keV Ar^+ ions under normal incidence for 10 min.

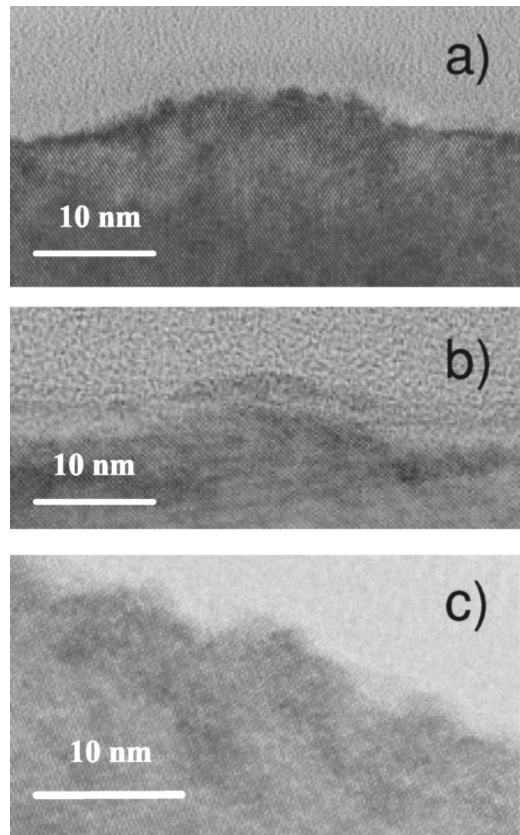


FIG. 4. Cross-sectional HRTEM image along the $\langle 110 \rangle$ direction for Si(001) surfaces bombarded under normal incidence with 1 keV Ar^+ ions for 10 min at (a) 375 K, (b) 425 K, and (c) 525 K.

B. High-resolution transmission electron microscopy (HRTEM)

Figures 4(a)–4(c) display HRTEM images obtained from Si(001) samples sputtered at 375, 425, and 525 K. These images show that the nanodots are composed of a crystalline core and an amorphous cover layer (1–2 nm). In Fig. 4(c), this cover amorphous layer can not be easily resolved due to the lack of contrast between this layer and the glue used to prepare cross-section specimens.

Qualitatively, the TEM images show that the size of the dots decreases in size with T . In particular, the smaller height and lateral size of the crystalline cores at 425 K is evident in comparison with that produced at 375 K. The evolution of the nanodots size has been quantified from statistical studies of low magnification TEM images. The range values obtained are gathered in Table I. In summary, the TEM analysis confirm that at 300–425 K the lateral size of the dots is clearly larger than in the 425–525 K range, as indicated by the AFM images. Note that at 525 K the dots still have a crystalline core.

C. Grazing incidence small angle x-ray scattering (GISAXS)

Figure 5 displays the GISAXS scans for Si(001) surfaces sputtered at different T . The measurements were performed at $\alpha_i=0.2^\circ$ and extracted from horizontal cuts corresponding at $\alpha_f=0.3^\circ$ in the 2D maps recorded with the CCD camera.

TABLE I. Dependence of the nanodots size (range values) with T derived from low magnification TEM images.

Temperature (K)	300 K	375 K	425 K	525 K
Average height (nm)	6–9	5–8	4–6	2–4
Average width (nm)	25–35	25–30	20–25	7–10

The correlation peaks on both sides of the reflected beam at $Q_y=0$ are related to the pattern formation, whose position is defined by the average interdot distance. It should be mentioned that during the GISAXS measurements there was an unavoidable parasitic scattering at low Q_y that decreases the contrast between the correlation peak and the background.

The correlation peak in the GISAXS scans is observed in all the Si(001) surfaces processed at temperatures up to 525 K. The decrease in its intensity reflects the progressive deterioration of ordering within the pattern, as already suggested by AFM. The position of the correlation peak indicates that the interdot distance stays constant at ~ 50 nm for temperatures up to 425 K. For higher temperatures, the dot distance decreases continuously down to ~ 30 nm. Extracting information by GISAXS about the dot morphology is not straightforward, since it requires complex fitting procedures. Therefore, in this point we should rely on the direct AFM and TEM data. Note that, in principle, potential tip convolution effects on the AFM data are not expected to influence the dot height values since the interdot distance is larger than the tip radius.

D. Grazing incidence diffraction (GID) at Si(220)

Figure 6(a) shows the evolution of the angular GID scans as a function of T . The pattern formation is derived from the

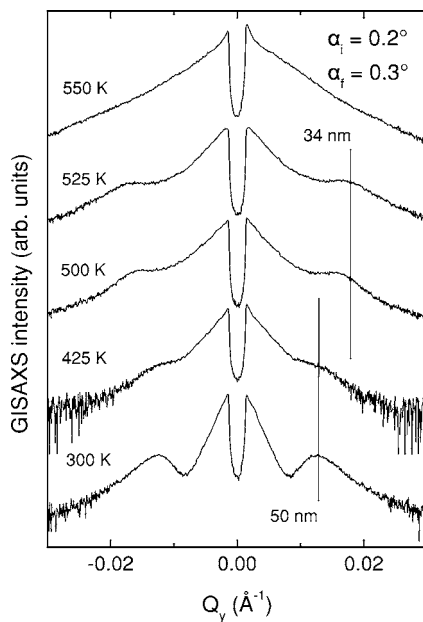


FIG. 5. GISAXS scans obtained from Si(001) substrates sputtered with 1 keV Ar⁺ ions for 10 min at 300, 425, 500, 525, and 550 K.

correlation peaks around the Si(220) Bragg reflection. The similar spectra at 300 and 375 K corroborate a low- T regime (up to 400 K) where T does not significantly affect the pattern formation. At 425 K, the correlation peak shifts slightly to higher Q values (i.e., shorter distances), in agreement with the trends observed by AFM and GISAXS. For temperatures above 475 K, the correlation peak disappears. At this T , the presence of a broad tail in the GID scan indicates the contribution of a form factor from crystalline dots, in agreement with the HRTEM observations from Fig. 4(c). These dots are uncorrelated since the correlation peak does not appear, probably due to the reason that not all the dots remain crystalline and, hence, they are randomly distributed.

Figure 6(b) shows the GID radial scans corresponding to the same samples as in Fig. 6(a). In this case, information about strain in the crystalline lattice of the dots can be also extracted. The asymmetry in the spectral shape indicates a change from tensile to compressive stress in the crystalline core of the dots between the low and high temperature regime. At higher T , the development of appreciable compressive strain ($\Delta a/a = -0.45\%$) is evident in Fig. 6(b), that is, when the dots decrease in size. This strain is too small to be detected in standard TEM studies but, accordingly to this trend, samples irradiated at higher temperatures (i.e., $T > 600$ K) indeed show in the TEM images (not shown here) clear strain effects in the near surface region.

The GID spectra in Fig. 6(a) for T above 375 K show a change in the slope at higher Q values, indicating a change in the form factor of the nanostructures. In particular, the

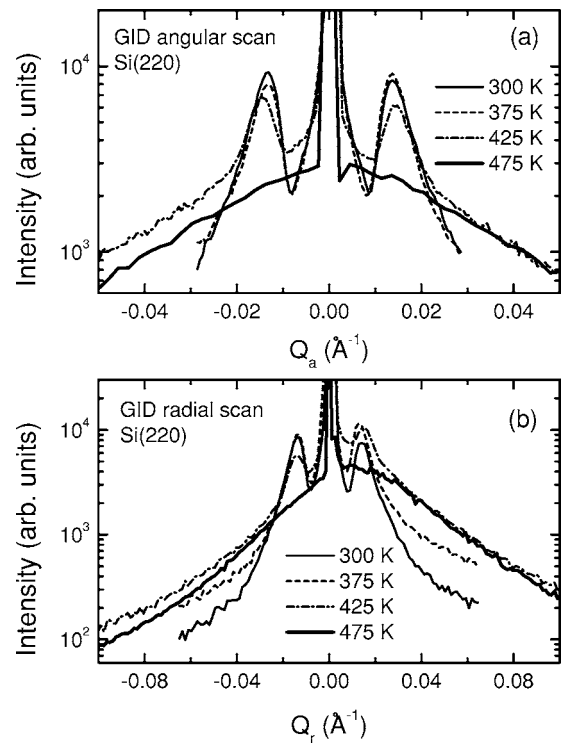


FIG. 6. GID measurements around the (220) in-plane Bragg peak in (a) angular and (b) radial directions from Si(001) substrates bombarded under normal incidence by 1 keV Ar⁺ ions for 10 min at 300 K (thin solid line), 375 K (dashed line), 425 K (dashed-dotted line), and 475 K (thick solid line).

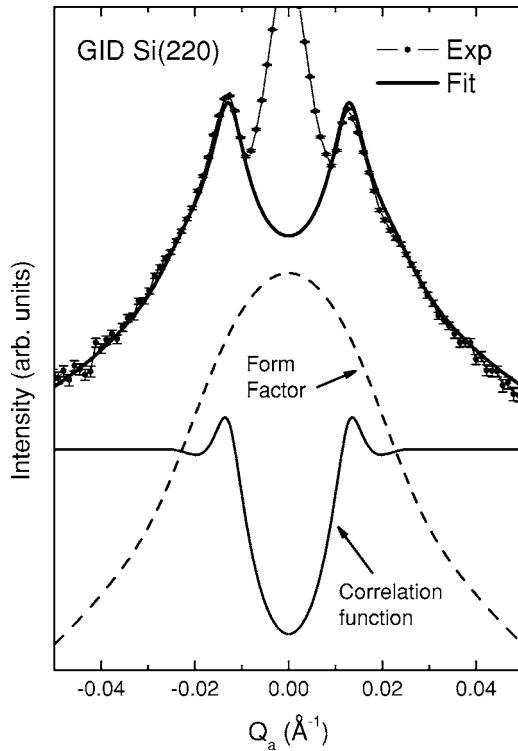


FIG. 7. Fitting analysis of the GID spectra considering the convolution of a form factor and a correlation function. The form factor of a cylinder has been considered for computation.

broader shape of the scan indicates a decrease in the lateral dimension of the crystalline core. This trend should be also related to the decrease in the dot height observed by AFM and TEM. In order to estimate the extent of this change, the GID spectra have been fitted considering a simplified cylindrical dot shape to calculate the form factor. The form factor also takes into account the size distribution of the dots. An example of the fitting procedure is depicted in Figure 7 for the sample produced at 300 K. Under the above assumption, the crystalline dot mean size is ~ 4 times smaller at 475 K than that at 300 K. This reduction in size is in agreement with the values from HRTEM shown in Table I.

V. DISCUSSION

A. Experimental observations

The temperature range (300–525 K) in which correlation, i.e., dot pattern formation, is observed by GISAXS is very consistent with the AFM data. This consistency could be expected from the fact that GISAXS is sensitive to the dot morphology independently of its crystallinity and, therefore, it probes the same structural properties as in the case of AFM, with a much higher statistical accuracy though. Differences between both techniques may be expected from the local character of AFM, whereas GISAXS averages over macroscopic dimensions (the GISAXS signal comes from a sampled area of $200 \mu\text{m}$ laterally and $\sim 1 \text{ mm}$ along the beam direction).

The comparison between GID and GISAXS is very informative since GID is only sensitive to the crystalline core of

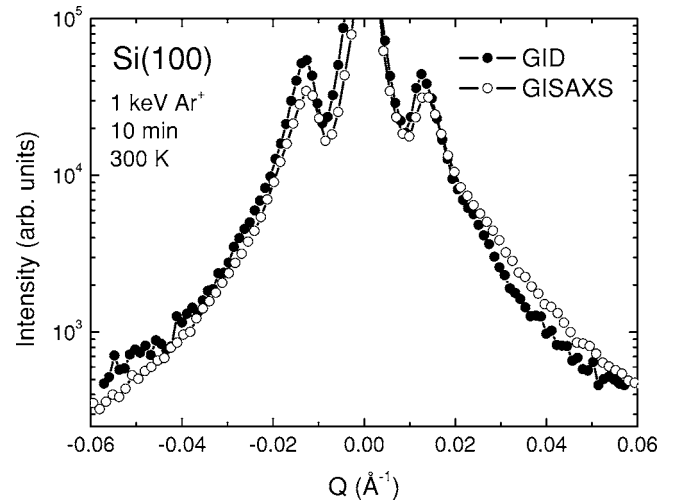


FIG. 8. Comparison of angular GID and GISAXS scans from a nanodot pattern produced on Si(001) by IBS with 1 keV Ar^+ ions for 10 min at 300 K.

the dots and their spatial correlation and, thus, the comparison yields the relative contribution of the crystalline core to the nanodot morphology. Figure 8 shows the comparison of the angular GID and GISAXS scans for the nanodots pattern produced at 300 K. Obviously, the correlation peak position from both techniques is the same, since it reflects the interdot distance. The very similar Q dependence of both scans indicates that the nanodots are mainly crystalline at this T , in agreement with HRTEM observations.¹⁹ As T increases, the evolution of the correlation peak in GISAXS and GID follows a similar trend. However, the correlation peak disappears at lower temperatures in GID (475 K) than in GISAXS (550 K), pointing out the increase in the relative contribution of the top-most amorphous layer to the dot morphology for $T > 400 \text{ K}$. Although the nanodots are still present at 475 K, the lack of correlation in GID at 475 K should be related to the reduced crystalline volume that contributes to the scattering signal. Note that, at this condition, the dot height is slightly larger than 2 nm and the thickness of the topmost amorphous layer is around 2 nm.¹⁹

Compiling all the experimental findings in this work, the production of Si nanodots by ion sputtering as a function of the substrate temperature can be described as follows. In the low- T range ($< 400 \text{ K}$), the pattern is not significantly affected by T and the interdot distance remains constant at $\sim 50 \text{ nm}$. Within the 425–500 K range, both the characteristic length and average height of the dot pattern decrease with T . This behavior continues up to 525 K, where an abrupt change of the surface morphology takes place. Still, a sort of dot morphology is present with dot height slightly larger than the crystalline dot core, as supported by the HRTEM images in Fig. 4 and the presence of a form factor in the GID spectra without correlation peak above 475 K in Fig. 6(a). However, now the dot does not have a clear lenticular shape and is not surrounded by a flat surface. In contrast, when T is further increased by only 25 K, the dot pattern completely vanishes. In this regime, the surface morphology becomes flat and dotless as assessed by HRTEM and AFM.

B. Comparison between experiment and theory

The experimental data reported in this work are, somehow, surprising within the BH and KS theoretical frameworks presented in Sec. II. In both equations, the temperature is included through the K contribution to the D term. Therefore, in the low temperature regime, the S contribution should prevail over K , implying that l_c should not depend on T . At increasing T , the weight of K should become more relevant and, therefore, the characteristic wavelength of the pattern, i.e., interdot distance, should scale with T ($l_c \sim \sqrt{K}$). In order to determine the influence of thermal diffusion mechanisms under our working conditions, the contributions of S and K can be computed using the equations introduced in Sec. II.

The maximum growth rate ($R_{k,\max}$) of the characteristic wavelength of the pattern is found to be $\sim 0.02 \text{ s}^{-1}$. As done in Ref. 25, this value is obtained by considering the evolution of the surface roughness with time, under similar ion bombardment conditions and at room temperature, from the data reported in Ref. 19. This value together with the input of the experimental wavelength of the pattern at room temperature ($l_c \sim 50 \text{ nm}$) lead to $\nu_{\text{exp}} \sim 2 \times 10^{-14} \text{ cm}^2 \text{ s}^{-1}$ and $D_{\text{exp}} \sim 8 \times 10^{-27} \text{ cm}^4 \text{ s}^{-1}$. In parallel, the ν and D values can be computed theoretically with Eq. (2), by assuming the microscopic quantities a , μ , and σ derived from the SRIM code.²⁶ The SRIM simulation code gives values of $a = 2.2 \text{ nm}$ (ion range calculated using the Bolse²⁷ approach as in Ref. 28), $\sigma = 1.3 \text{ nm}$, and $\mu = 1.9 \text{ nm}$. These parameters give the theoretical values of $\nu_{\text{th}} \sim 6 \times 10^{-15} \text{ cm}^2 \text{ s}^{-1}$ and $S_{\text{th}} \sim 5 \times 10^{-29} \text{ cm}^2 \text{ s}^{-1}$, being in good agreement (considering orders of magnitude) with the ones calculated from experimental values. It should be also taken into account that SRIM simulations are not completely reliable, since usually SRIM underestimates the value of the lateral straggling and even that of the longitudinal straggling.²⁵

In order to evaluate the weight of the contribution of the thermal self-diffusion term, the value of $D_s C$ has to be estimated, i.e., the diffusion activation energy, ΔE , and the concentration of mobile species, C . Among the mobile species, the most likely are monomers and dimers,²⁹ which have different ΔE values. Besides, the strain present in the system can also affect the value of ΔE .³⁰ Thus, in the literature a relatively wide range of ΔE values is found depending on the system conditions, most of them being in the 1–2.4 eV range.^{29,31,32} For instance, the only report providing a ΔE value for low energy ion bombarded Si(001) surfaces at temperatures in the 730–870 K range, obtained $\Delta E \sim 1.2 \text{ eV}$.²¹ Thus, a reasonable and safe assumption for our computation can be to consider an average value of $\Delta E \sim 1 \text{ eV}$. Then, for a typical concentration of mobile species of $C \sim 0.05$ and adding the parameters for the Si(001) surface ($d = 0.389 \text{ nm}$, $f \sim 10^{13} \text{ Hz}$, $\gamma = 7.7 \text{ eV/nm}^2$, and $\Omega = 0.02 \text{ nm}^3/\text{at.}$),²¹ we obtain a value of $K(300 \text{ K}) \sim 4 \times 10^{-36} \text{ cm}^4 \text{ s}^{-1}$ at room temperature.

The calculated K value should be considered, rather, as an estimate due to the simplifying assumptions made. The important fact is that K is several orders of magnitude lower than D_{exp} . This fact confirms the predominance for our system of ion-induced diffusion near room temperature, which

is consistent with the observed constant interdot distance of $\sim 50 \text{ nm}$ up to $\sim 400 \text{ K}$. This behavior was also observed for GaSb nanodots produced by IBS in the temperature range of 213–333 K.⁹ From the K value and the temperature dependence of K , we can also estimate that thermal self-diffusion should start to compete with the ion-induced diffusion at $T \sim 900 \text{ K}$, well above the temperature window sampled in this work. Therefore, in our high temperature range, the changes observed in our experiments above $\sim 400 \text{ K}$ shown in Fig. 3(c) cannot be related to thermal-induced diffusion processes since the latter should become predominant at much higher temperatures. Moreover, the observed behavior for the pattern wavelength for $T > 400 \text{ K}$ is the opposite of that expected if thermal-induced diffusion processes govern the pattern dynamics. This contrasts with the reported^{33,34} trends for ripple formation on Si(001), where a behavior in agreement with the predictions from thermal diffusion was observed, but it should be noted that the ripple patterns were produced at $T > 773 \text{ K}$ and that, in this temperature range, no dot pattern has been obtained on Si under our experimental conditions. Although the trend reported here is surprising, the reproducibility of these results has been carefully checked by repeating several times the present experiment and even using different IBS devices. Moreover, there are similar observations made by Chini *et al.* on ripple production on Si(001) surfaces by 60 keV Ar⁺ bombardment with and without simultaneous scanning of the implanter beam.³⁵ Interestingly, when the beam scanning is suppressed, the wavelength of ripple patterns shows a negative exponent in the dependence with ion energy and, for a given energy value, it decreases with respect to the value obtained with beam scanning. Since the sample reaches a higher temperature without beam scanning, this behavior was related by the authors to a temperature effect. Under this scenario, the pattern wavelength shows a larger decrease when the ion energy increases, i.e., when the sample temperature is higher, in qualitative agreement with our observations.

The results shown here point out that the theoretical understanding of pattern formation by IBS is far from being fully understood. The observed trend with T suggests that there are additional thermally-driven mechanisms under IBS operating at lower temperatures than diffusion. A plausible approach could be considering the “hydrodynamic” model proposed by Castro *et al.*¹⁴ instead of the BH framework since in Eq. (4) T appears in coefficients different from the D term (contrary to the BH, KS, and DKS equations). Although the influence of T through these terms might be expected to lead, for appropriate parameter values, to a behavior similar to that observed in the present experiments, preliminary analysis seems to lead to the opposite conclusion.³⁶ Nevertheless, detailed study of the role played by T on the induced pattern being very complex, theoretical work is in progress. Moreover, additional physical effects³⁶ might be influencing the present temperature dependence, which are not taken into account in the previous theoretical models. First, recrystallization at high T may counteract the ion-induced amorphization³⁴ and, therefore, the assumption in which continuum models rely, i.e., the amorphous state of the surface, is not valid anymore. This effect has been supported by the seemingly different pattern properties reported for IBS on

Si(111) in Ref. 34 from those predicted in Ref. 14. Second, the slope of the (log-log) PSD curves at small wave vectors in Fig. 2 seems reminiscent of bulk viscous flow relaxation effects³⁷ analogous of those previously considered in IBS of silica at off-normal incidence.³⁸ Since, when present, such effects dominate asymptotically and are stabilizing in nature, they might also account for the disappearance of the pattern at high enough T . However, at this point we do not have information (even approximate) on the dependence of the parameters that mediate this mechanism (namely, surface tension and viscosity) with T for our experimental system, and remain unable to account for the change of pattern characteristics with T before its disappearance for our highest T values. Finally, as mentioned, a change in the surface diffusion can also be induced by the presence of strain fields on the surface.³⁰ As shown in our GID data, the decrease in the characteristic wavelength of the pattern is accompanied by a progressive increase of a compressive strain in the near surface region. It has been reported that a compressive (or tensile) strain can either increase or decrease the surface diffusion, depending on whether the adatom-induced surface stress is under tension or compression.³⁰ Therefore, an eventual reduction in the surface diffusivity due to the presence of strain could also explain the observed decrease in the characteristic wavelength.

At this point, we would like to highlight the complexity of pattern formation by IBS. This fact is evident both experimentally (especially in the case of Si, where the ion beam properties³⁹ and sample environment⁴⁰ seem to play a determinant role) and theoretically. Reliable experimental data are needed to contrast the different theoretical approaches and it is clear that the models have to be further extended and developed in order to account for the large variety of experimental observations. In particular, at this stage, there is not a clear relationship between most of the coefficients governing the terms in continuum models and the surface material properties that can account for the widely different pattern

properties produced by IBS, for instance, on Si, InP, and GaSb surfaces.

VI. CONCLUSIONS

We have shown that nanodot patterns can be produced by IBS of Si(001) at different values of T , allowing control over the nanodot morphology and pattern characteristics. In particular, three different T regimes are observed. First, the pattern remains unaltered for $T \leq 400$ K, with the dot volume mostly crystalline. Second, there is a progressive decrease in the dot height for an increase in the temperature from 400 K up to 500 K, which implies a higher contribution of the amorphous surface layer on the dot morphology. At the same time, there is an increase in the compressive strain within the crystalline core of the dots as T increases. Finally, for $T \geq 550$ K the nanostructures disappear and the surface becomes featureless and flat. Aside from the technological implications of the control on the pattern characteristics, this evolution has been discussed in the framework of existing theoretical models dealing with the morphology of ion sputtered surfaces. This analysis points out the need of additional experimental and theoretical work to understand the complex process of surface nanopatterning by IBS.

ACKNOWLEDGMENTS

We are strongly indebted to J. Muñoz, M. Castro, and R. Cuerno for fruitful discussions and suggestions. We also thank H. Djazouli for his technical support at the ESRF. This work has been partially supported by Grants Nos. BFM-2003-07749-C02 and ESP-2002-04509-C04-01 from the Spanish Ministerio de Educación y Ciencia (MEC) and Grant No. GR-MAT-0431-2004 from the Comunidad Autónoma de Madrid. R.G. and J.A.S. acknowledge the financial support from the Spanish MEC through the “Ramón y Cajal” program and the Spanish CSIC, respectively.

*Corresponding author. Present address: Centro de Micro-Análisis de Materiales, Universidad Autónoma De Madrid, c/Faraday 3 (Edificio 22), Campus de Cantoblanco, 28049 Madrid Spain. Electronic address: raul.gago@uam.es

†Present address: Oak Ridge National Laboratory, Oak Ridge, Tennessee 37830-6031, USA.

¹T. Shimizu-Iwayama, S. Nakao, and K. Saitoh, *Appl. Phys. Lett.* **65**, 1814 (1994) 1814.

²*Springer Handbook of Nanotechnology*, edited by B. Bhushan (Springer-Verlag, Berlin, 2004).

³J. Stangl, V. Holy, and G. Bauer, *Rev. Mod. Phys.* **76**, 725 (2004).

⁴U. Valbusa, C. Boragno, and F. Bautier de Mongeot, *J. Phys.: Condens. Matter* **14**, 8153 (2002).

⁵M. Navez, C. Sella, and D. Chaperot, *Acad. Sci., Paris, C. R.* **254**, 240 (1962).

⁶S. Facsko, T. Dekorsy, C. Koerdt, C. Trappe, H. Kurz, A. Vogt, and H. L. Hartnagel, *Science* **285**, 1551 (1999).

⁷F. Frost, A. Schindler, and F. Bigl, *Phys. Rev. Lett.* **85**, 4116 (2000).

⁸J. J. Vajo, R. E. Doty, and E.-H. Cirlin, *J. Vac. Sci. Technol. A* **14**, 2709 (1996).

⁹S. Facsko, T. Dekorsy, and H. Kurz, *Phys. Rev. B* **63**, 165329 (2001).

¹⁰R. M. Bradley and J. M. E. Harper, *J. Vac. Sci. Technol. A* **6**, 2390 (1988).

¹¹R. Cuerno and A.-L. Barabási, *Phys. Rev. Lett.* **74**, 4746 (1995).

¹²M. A. Makeev, R. Cuerno, and A.-L. Barabási, *Nucl. Instrum. Methods Phys. Res. B* **197**, 185 (2002).

¹³B. Kahng, H. Jeong, and A.-L. Barabási, *Appl. Phys. Lett.* **78**, 805 (2001).

¹⁴M. Castro, R. Cuerno, L. Vázquez, and R. Gago, *Phys. Rev. Lett.* **94**, 016102 (2005); M. Castro and R. Cuerno, *ibid.* **94**, 139601 (2005); J. Muñoz-García, M. Castro, and R. Cuerno, *ibid.* **96**, 086101 (2006).

¹⁵S. Facsko, T. Bobek, A. Stahl, H. Kurz, and T. Dekorsy, *Phys.*

- Rev. B **69**, 153412(R) (2004).
- ¹⁶S. Vogel and S. J. Linz, Phys. Rev. B **72**, 035416 (2005).
- ¹⁷M. A. Makeev and A.-L. Barabási, Appl. Phys. Lett. **71**, 2800 (1997).
- ¹⁸F. Frost, B. Ziberi, T. Höche, and B. Rauschenbach, Nucl. Instrum. Methods Phys. Res. B **216**, 9 (2004).
- ¹⁹R. Gago, L. Vázquez, R. Cuerno, M. Varela, C. Ballesteros, and J. M. Albella, Appl. Phys. Lett. **78**, 3316 (2001).
- ²⁰R. Gago, L. Vázquez, R. Cuerno, M. Varela, C. Ballesteros, and J. M. Albella, Nanotechnology **13**, 304 (2002).
- ²¹J. Erlebacher, M. J. Aziz, E. Chason, M. B. Sinclair, and J. A. Floro, J. Vac. Sci. Technol. A **18**, 115 (2000).
- ²²P. Sigmund, Phys. Rev. **184**, 383 (1969).
- ²³T. Aste and U. Valbusa, Physica A **332**, 548 (2004).
- ²⁴V. Holý, U. Pietsch, and T. Baumbach, *High-Resolution X-Ray Scattering from Thin Films and Multilayers* (Springer-Verlag, Berlin, 1999).
- ²⁵T. Bobek, S. Facsko, H. Kurz, T. Dekorsy, M. Xu, and C. Teichert, Phys. Rev. B **68**, 085324 (2003).
- ²⁶J. F. Ziegler, J. P. Biersack, and U. Littmark, *The Stopping and Range of Ions in Solids* (Pergamon, New York, 1985).
- ²⁷W. Bolse, Mater. Sci. Eng., R. **12**, 53 (1994).
- ²⁸B. Ziberi, F. Frost, Th. Höche, and B. Rauschenbach, Phys. Rev. B **72**, 235310 (2005).
- ²⁹B. S. Swartzentruber, Phys. Rev. Lett. **76**, 459 (1996).
- ³⁰D. J. Shu, F. Liu, and X. G. Gong, Phys. Rev. B **64**, 245410 (2001).
- ³¹R. M. Tromp and M. Mankos, Phys. Rev. Lett. **81**, 1050 (1998).
- ³²M. E. Keeffe, C. C. Umbach, and J. M. Blakely, J. Phys. Chem. Solids **55**, 965 (1994).
- ³³J. Erlebacher, M. J. Aziz, E. Chason, M. B. Sinclair, and J. A. Floro, Phys. Rev. Lett. **82**, 2330 (1999).
- ³⁴A.-D. Brown and J. Erlebacher, Phys. Rev. B **72**, 075350 (2005).
- ³⁵T. K. Chini, M. K. Sanyal, and S. R. Bhattacharyya, Phys. Rev. B **66**, 153404 (2002).
- ³⁶J. Muñoz-García, M. Castro, and R. Cuerno (private communication).
- ³⁷J. Muñoz-García, M. Castro, and R. Cuerno (private communication).
- ³⁸T. Mayer, E. Chason, and A. J. Howard, J. Appl. Phys. **76**, 1633 (1994).
- ³⁹B. Ziberi, F. Frost, M. Tartz, H. Neumann, and B. Rauschenbach, Thin Solid Films **459**, 106 (2004).
- ⁴⁰G. Ozaydin, A. S. Özcan, Y. Wang, K. F. Ludwig, H. Zhou, R. L. Headrick, and D. P. Siddons, Appl. Phys. Lett. **87**, 163104 (2005).